

NaLaW₂O₇(OH)₂(H₂O): Crystal Structure and RE³⁺ Luminescence in the Pristine and Annealed Double Tungstates (RE = Eu, Tb, Sm, and Dy)

Xuejiao Wang,^{†,‡,§,||} Xiaofei Shi,^{‡,§,||} Maxim S. Molokeev,^{*,†,‡,§,||,@} Zhihao Wang,^{‡,§,||} Qi Zhu,^{§,||} Xiaodong Li,^{§,||} Xudong Sun,^{§,||} and Ji-Guang Li^{*,‡,§,||}

[†]College of New Energy, Bohai University, Jinzhou, Liaoning 121007, China

[‡]Research Center for Functional Materials, National Institute for Materials Science, Tsukuba, Ibaraki 305-0044, Japan

[§]Key Laboratory for Anisotropy and Texture of Materials (Ministry of Education), Northeastern University, Shenyang, Liaoning 110819, China

^{||}Institute of Ceramics and Powder Metallurgy, School of Materials Science and Engineering, Northeastern University, Shenyang, Liaoning 110819, China

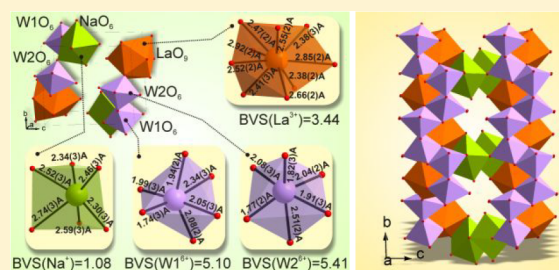
[†]Laboratory of Crystal Physics, Kirensky Institute of Physics, Federal Research Center KSC SB, Russian Academy of Sciences, Krasnoyarsk 660036, Russia

[#]Department of Physics, Far Eastern State Transport University, Khabarovsk 680021, Russia

[@]Siberian Federal University, Krasnoyarsk 660041, Russia

Supporting Information

ABSTRACT: Hydrothermal reaction of La(NO₃)₃ and Na₂WO₄·2H₂O at 100 °C and pH 8 resulted in the formation of new compound NaLaW₂O₇(OH)₂(H₂O), as confirmed by the X-ray diffraction results, chemical composition, Fourier transform infrared, thermogravimetric/differential thermal analysis, and transmission electron microscopy analyses. The crystal structure was determined in the triclinic system (space group *P* $\bar{1}$), with lattice constants *a* = 5.8671(2) Å, *b* = 8.2440(2) Å, and *c* = 9.0108(3) Å, axis angles α = 93.121(2)°, β = 75.280(2)°, and γ = 94.379(2)°, and cell volume *V* = 420.03(2) Å³. The structure contains two-dimensional layers of



-(W₁O₆)-(W₁O₆)-(W₂O₆)-(W₂O₆)-(W₁O₆)-(W₁O₆)- and -LaO₉-LaO₉- chains alternating in the *a*–*b* plane, which are linked together through NaO₆ octahedral trigonal prisms by edges to form a three-dimensional net. Dehydration of the compound proceeds up to a low temperature of ~350 °C and results in the formation of technologically important NaLa(WO₄)₂ double tungstate, which is thus a unique precursor for the latter. Na(La,RE)W₂O₇(OH)₂(H₂O) and Na(La,RE)(WO₄)₂ solid solutions separately doped with the practically important activators for which RE = Eu, Tb, Sm, and Dy were also successfully synthesized and investigated for their structural features and photoluminescence properties, including excitation, emission, quantum yield, emission color, and fluorescence decay kinetics. The compounds were shown to exhibit dominantly strong red (~616 nm for Eu³⁺; λ_{ex} = 395 or 464 nm), green (~545 nm for Tb³⁺; λ_{ex} = 278 or 258 nm), deep red (~645 nm for Sm³⁺; λ_{ex} = 251 nm), and yellow (~573 nm for Dy³⁺; λ_{ex} = 254 nm) emission upon being irradiated with the peak wavelengths of their strongest excitation bands.

1. INTRODUCTION

The rare-earth (RE) double tungstates of ARE(WO₄)₂ (A = alkali metal ion) initially attracted attention for solid laser applications in the single-crystal form, because of their excellent mechanical, thermal, and chemical durability, the high value of the $\chi^{(3)}$ nonlinear cubic susceptibility, their good Raman activity, the facile admittance of various RE³⁺ activators, and the broad optical transparency from the visible to the near-infrared region.^{1–8} Later studies revealed that ARE(WO₄)₂ tungstates (RE = La, Y, Gd, and Lu) are attractive hosts for luminescent purposes,^{9,10} because these RE³⁺ ions do not have absorption or emission in the visible light region and

the compounds present self-activation of the WO₄²⁻ ligands,¹⁰ high optical absorption in the ultraviolet (UV) region, and efficient energy transfer from WO₄²⁻ to the activator.^{11–13} The potential application of ARE(WO₄)₂ has been demonstrated in the multifaceted areas of bioimaging [PEG-NaGd(WO₄)₂:Eu],¹⁴ biosensors [Na(Gd,Eu)(WO₄)₂],¹⁵ photothermal therapy (PTT) [NaY(WO₄)₂:Sm³⁺/Nd³⁺],¹⁶ photocatalysis,¹⁷ light-emitting diodes (LEDs) [NaGd(WO₄)₂:Pr³⁺],¹⁸ and temperature sensing [NaY(WO₄)₂:Er³⁺/Yb³⁺].¹⁹

Received: August 6, 2018

Published: October 17, 2018

The synthesis of $\text{ARE}(\text{WO}_4)_2$ compounds can be achieved by a number of methodologies, including solid-state reaction,¹⁸ sol-gel and Pechini-type sol-gel,⁹ molten salt growth,²⁰ microwave-assisted processing^{21,22} and hydrothermal/solvothermal reaction,^{10,23} as also summarized in the review article by Kaczmarek and van Deun.²⁴ Though the hydrothermal and solvothermal techniques are widely acknowledged to be capable of directly generating inorganic solids of controlled phase structure and crystallite morphology within a short amount of reaction time, they frequently yielded unknown products (precursors) for the RE^{3+} -tungstate reaction system. As a result, subsequent annealing is needed to convert the precursor into the targeted $\text{ARE}(\text{WO}_4)_2$:Ln compound ($A = \text{Na}$ and K ; $\text{RE} = \text{La}$, Y , Gd , and Lu ; $\text{Ln} = \text{Eu}^{3+}$, Tb^{3+} , Sm^{3+} , Dy^{3+} , and $\text{Sm}^{3+}/\text{Nd}^{3+}$; etc.).^{5,9,16,25} This is primarily due to the rich solution chemistry of tungstate anions, which present themselves as monomeric $[\text{WO}_4]^{2-}$ in a solution of sufficiently high alkalinity ($\text{pH} > 8$), while the various protonated and polymerized forms of $[\text{H}_{18}(\text{WO}_4)_{12}]^{6-}$, $[\text{H}_{10}(\text{WO}_4)_6]^{2-}$, $[\text{H}_7(\text{WO}_4)_6]^{5-}$, and $[\text{HWO}_4]^-$ appear in an acidic or neutral solution ($\text{pH} 4\text{--}7$).^{26–35} Furthermore, the type and concentration of tungstate ions are affected by not only the solution pH but also the temperature, the initial concentration of the tungstate source (such as $\text{Na}_2\text{WO}_4 \cdot 2\text{H}_2\text{O}$ in this work), and the attendance and concentration of alien anions. On the other hand, RE^{3+} undergoes hydration and hydrolysis in an aqueous solution to form $[\text{RE}(\text{OH})_x(\text{H}_2\text{O})_y]^{3-x}$ complex ions, whose x value increases with an increase in the solution pH.^{36,37} Numerous reaction pathways are, therefore, possible under hydrothermal/solvothermal conditions, which, in turn, make the product rather sensitive to the synthesis parameter.^{27,38,39} It was recently shown that the reactivity of tungstate species toward $[\text{RE}(\text{OH})_x(\text{H}_2\text{O})_y]^{3-x}$ decreases with an increase in solution pH, and the hydrothermal product of a higher pH tends to have a lower W/RE molar ratio and vice versa.^{26,27} The complicated solution chemistry and reaction pathway may account for why most of the studies to date left the hydrothermal/solvothermal precursors unanalyzed for chemical composition, phase purity, phase constituent, and phase structure. Nevertheless, successful examples do exist for the direct crystallization of $\text{ARE}(\text{WO}_4)_2$ via hydrothermal and solvothermal reactions. Liu et al., for example, produced $\text{NaLa}(\text{WO}_4)_2 \cdot \text{Er}^{3+}/\text{Eu}^{3+}$ and $\text{NaGd}(\text{WO}_4)_2 \cdot \text{Tm}^{3+}/\text{Dy}^{3+}/\text{Eu}^{3+}$ via one-step hydrothermal reaction at 180°C for 20 h,^{10,40} and Wang et al. obtained $\text{NaLa}(\text{WO}_4)_2 \cdot \text{Ln}^{3+}$ via solvothermal (ethylene glycol as the co-solvent) and hydrothermal reactions at $160\text{--}200^\circ\text{C}$ for 12 h.⁴¹

In our efforts to crystallize $\text{NaLa}(\text{WO}_4)_2$ via hydrothermal reaction of Na_2WO_4 and $\text{La}(\text{NO}_3)_3$, we encountered an unknown precursor that can be dehydrated to $\text{NaLa}(\text{WO}_4)_2$ by calcination in air at the very low temperature of $\sim 350^\circ\text{C}$. Thus, we performed a comprehensive characterization of the precursor with the combined techniques of elemental analysis, Fourier transform infrared (FTIR), thermogravimetric/differential thermal analysis (TG/DTA), X-ray diffraction (XRD), field emission scanning electron microscopy (FE-SEM), and transmission electron microscopy (TEM) and confirmed that it is a new compound $\text{NaLaW}_2\text{O}_7(\text{OH})_2(\text{H}_2\text{O})$, whose crystal structure was originally analyzed to belong to the triclinic system (space group $P\bar{1}$) and to feature $-(\text{W}1\text{O}_6)-(\text{W}1\text{O}_6)-(\text{W}2\text{O}_6)-(\text{W}2\text{O}_6)-(\text{W}1\text{O}_6)-(\text{W}1\text{O}_6)-$ and $-\text{LaO}_9-\text{LaO}_9-$ polyhedral chains alternating in the a - b plane. Doping the compound with the practically important activators of Eu^{3+} ,

Tb^{3+} , Sm^{3+} , and Dy^{3+} was also successful. We, therefore, report in this work our detailed characterization and structural analysis of the compound, together with the photoluminescence properties of the aforementioned activators in both the pristine $\text{NaLaW}_2\text{O}_7(\text{OH})_2(\text{H}_2\text{O})$ and calcination-derived $\text{NaLa}(\text{WO}_4)_2$ double tungstates. Our synthesis studies also revealed that $\text{NaLnW}_2\text{O}_7(\text{OH})_2(\text{H}_2\text{O})$ tends to crystallize via hydrothermal reaction for the large Ln^{3+} ions of $\text{Ln} = \text{La}\text{--}\text{Nd}$ in the lanthanide series. We believe that the outcome of this work may enrich our understanding of the $\text{RE}^{3+}\text{--}\text{WO}_4^{2-}$ reaction and have wide implications for the hydrothermal crystallization of other RE tungstates and even molybdate analogues.

2. EXPERIMENTAL SECTION

2.1. Reagents and Sample Synthesis. The 99.99% pure $\text{Ln}(\text{NO}_3)_3 \cdot 6\text{H}_2\text{O}$ ($\text{Ln} = \text{La}$, Sm , Eu , Tb , and Dy), analytical grade sodium tungstate dihydrate ($\text{Na}_2\text{WO}_4 \cdot 2\text{H}_2\text{O}$), NaOH , and HNO_3 were purchased from Kanto Chemical Co., Inc. (Tokyo, Japan), and were used without further purification. Milli-Q filtered water (resistivity of $\sim 18 \text{ M}\Omega \text{ cm}$) was used throughout the experiments. The synthesis of the crystalline $\text{NaLaW}_2\text{O}_7(\text{OH})_2(\text{H}_2\text{O})$ product was performed by the following procedure.²³ First, 6 mL of a Na_2WO_4 solution (1.0 mol/L) was dropwise added to 20 mL of a $\text{La}(\text{NO}_3)_3$ solution (0.1 mol/L; 3:1 $\text{WO}_4^{2-}:\text{La}^{3+}$ molar ratio) under magnetic stirring at room temperature, followed by adjusting the pH with dilute NaOH and HNO_3 solutions to 8 while keeping the total volume at 70 mL. After homogenization for 30 min, the mixture was transferred to a Teflon-lined stainless steel autoclave with a 100 mL capacity for reaction for 24 h in an electric oven preheated to 100°C . After naturally cooling to room temperature, the hydrothermal product was collected via centrifugation, washed with water three times, rinsed with absolute ethanol, and then dried in an oven at 70°C for 24 h in air. The activator-doped compounds of $\text{Na}(\text{La}_{1-x}\text{RE}_x)\text{W}_2\text{O}_7(\text{OH})_2(\text{H}_2\text{O})$ ($x = 0.05$ for $\text{RE} = \text{Eu}$ and Tb and $x = 0.02$ for $\text{RE} = \text{Sm}$ and Dy) were synthesized using the protocol described above. The lower doping levels of Sm^{3+} and Dy^{3+} are considered from their substantially more abundant energy levels, which cause easier concentration quenching of luminescence. Calcination of the hydrothermal product was conducted in air at 500°C for 2 h, with a heating rate of $5^\circ\text{C}/\text{min}$ at the ramp stage.

2.2. Characterization. Phase identification was performed by X-ray diffraction (XRD, Smart Lab3, Rigaku, Tokyo, Japan) at 40 kV, 40 mA, and room temperature, using nickel-filtered $\text{Cu K}\alpha$ radiation (wavelength of 0.15406 nm) and a scanning speed of $4.0^\circ 2\theta \text{ min}^{-1}$. For crystal structure analysis, the sample was ground with a zirconia mortar and pestle to avoid the possible influence of the orientation, and the XRD data were collected in the step-scan mode with a step size of 0.02° and an accumulation time of 10 s. The Rietveld refinement was carried out using TOPAS version 4.2.⁴² The photoluminescence spectra, fluorescence decay kinetics, and quantum efficiency of the as-synthesized $\text{Na}(\text{La}_x\text{RE}_{1-x})\text{W}_2\text{O}_7(\text{OH})_2(\text{H}_2\text{O})$ and calcination-derived $\text{Na}(\text{La}_x\text{RE}_{1-x})\text{WO}_4$ were recorded at room temperature with an FP-6500 fluorospectrophotometer (Jasco, Tokyo, Japan) equipped with a 150 W xenon lamp for excitation and a $\Phi 60$ mm integrating sphere (model ISF-834, Jasco). A scan speed of 100 nm/min and slit widths of 5 nm for both excitation and emission were used. The spectral responses of the spectrophotometer were corrected in the range of 200–850 nm with a Rhodamine-B solution (5.5 g/L in ethylene glycol, for the 200–600 nm spectral region) and with a standard light source unit (ECS-333, Jasco, for the 350–850 nm region) as references. The quantum efficiency of luminescence was analyzed with the built-in software of the spectrophotometer by comparing the response of the phosphor to excitation with a Spectralon diffusive white standard. The morphology and microstructure of the product were analyzed via FE-SEM (model S-4800, Hitachi, Tokyo, Japan) at an acceleration voltage of 10 kV and TEM (model JEM-2100F, JEOL, Tokyo, Japan) at 200 kV. FTIR

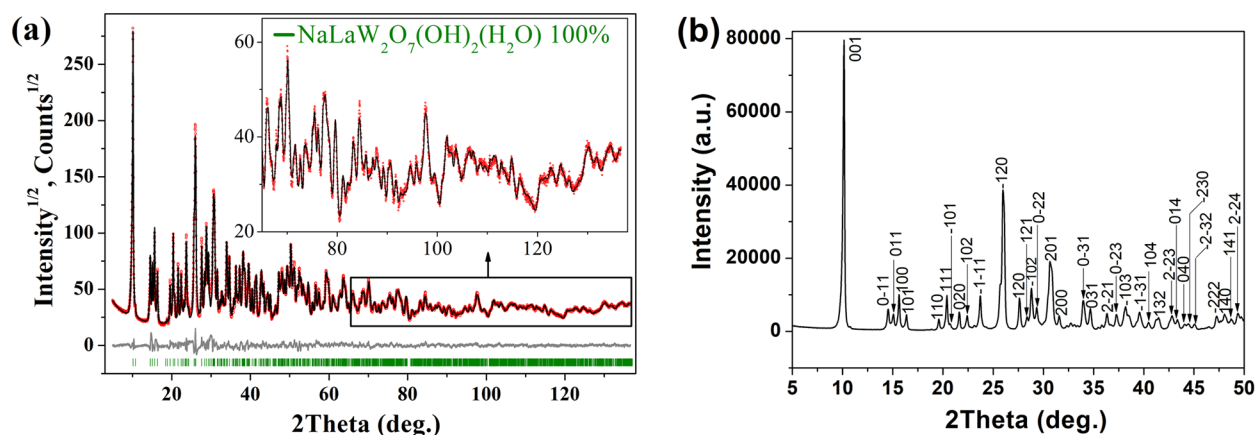


Figure 1. (a) Difference Rietveld plot of $\text{NaLaW}_2\text{O}_7(\text{OH})_2(\text{H}_2\text{O})$ and (b) indexing of the XRD peaks in the $2\theta = 5\text{--}50^\circ$ region. The observed pattern is shown by the black solid line. The calculated data are shown by the red dots. The positions of Bragg reflections are indicated by the green tick marks. The difference between the results of the experiment and calculation is given by the gray line.

spectroscopy (model FT/IR-4200, Jasco) was performed by the KBr pellet method following standard procedures. The contents of the constituent elements were determined for the product via inductively coupled plasma (ICP) spectroscopy for W and La on an IRIS Advantage analyzer (Jarrell-Ash Japan, Kyoto, Japan), for Na on an SPS3520UV-DD instrument (SHI Technologies Inc., Tokyo, Japan), and for O via the inert gas fusion–infrared absorptiometry technique (model TC-436, LECO, St. Joseph, MI). TG/DTA (Thermal plus TG 8120, Rigaku) was performed in stagnant air with a heating rate of $10^\circ\text{C}/\text{min}$.

3. RESULTS AND DISCUSSION

3.1. Characterization and Crystal Structure Analysis of the Hydrothermal Product. Elemental analysis indicates that the product obtained via hydrothermal crystallization at 100°C and pH 8 for 24 h contains 3.2 ± 0.1 wt % Na, 19.7 ± 0.1 wt % La, 52.1 ± 0.2 wt % W, and 21 ± 1 wt % O, which closely correspond to a Na:La:W:O molar ratio of 1.0:1.0:2.0:9.4. The XRD pattern of the product is shown in Figure 1. The sharp reflections indicate the highly crystalline nature of the sample, but indexing the pattern with currently available diffraction data and references failed. This unknown phase can, however, be well indexed using TOPAS version 4.2⁴² in the triclinic unit cell with the following parameters: $a = 5.864 \text{ \AA}$, $b = 8.230 \text{ \AA}$, $c = 9.002 \text{ \AA}$, $\alpha = 93.05^\circ$, $\beta = 75.27^\circ$, $\gamma = 94.357^\circ$, and $V = 418.70 \text{ \AA}^3$ (goodness of fit of 21.41). Two allowed space groups of $P1$ and $P\bar{1}$ were considered, and $P\bar{1}$, differing in its higher symmetry, was initially chosen. The structure was determined by modeling in direct space followed by simulated annealing using FOX.⁴³ One La^{3+} ion, two W^{6+} ions, and one Na^+ ion were generated, and a dynamic population of positions was used for all of the atoms.⁴² The thus obtained model of the structure was refined using Rietveld refinement in TOPAS version 4.2. The difference plot of electron density based on $F_{\text{obs}} - F_{\text{calc}}$, where F_{obs} and F_{calc} are observed and calculated structural amplitudes, respectively, was used to localize all O^{2-} ions, and 10 independent O sites were found. Two Na^+ , two La^{3+} , four W^{6+} , and 20 O^{2-} ions were found in the unit cell, and thus, the compound can be nominally written as $\text{NaLaW}_2\text{O}_{10}$. The formula, however, has a negative charge sum of -4 , and therefore, some of the O^{2-} ions should be OH^- ions or H_2O molecules. Three probable chemical formulas of $\text{NaLaW}_2\text{O}_8(\text{H}_2\text{O})_2$, $\text{NaLaW}_2\text{O}_7(\text{OH})_2(\text{H}_2\text{O})$, and $\text{NaLaW}_2\text{O}_6(\text{OH})_4$ can then be

generated. Unfortunately, after refinement with all O sites using the anisotropic model of preferred orientation with spherical harmonics of the second order, the difference electron map did not help to localize hydrogen atoms, and the chemical formula of the product could not be directly determined. To gain a better understanding of the chemical formula, the local structure of all 10 O sites was instead investigated.

Figure 2 shows the coordination spheres of all 10 O sites that were divided into three groups. The first group consists of

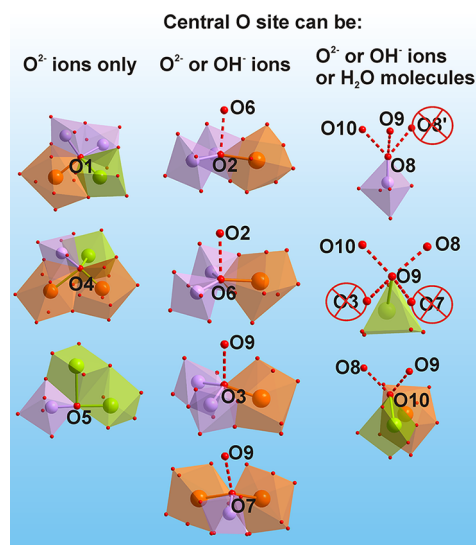


Figure 2. Three groups of coordination spheres of all 10 O sites. The crossed out O sites cannot be considered as a direction of an $\text{O}\cdots\text{H}\cdots\text{O}$ hydrogen bond due to different geometric restrictions. The orange, purple, and green polyhedra represent LaO_9 , $(\text{W}1/\text{W}2)\text{O}_6$, and NaO_6 , respectively.

$\text{O}1$, $\text{O}4$, and $\text{O}5$ sites that can be coordinated with only metal ions and correspond to O^{2-} ions. The second group contains $\text{O}2$, $\text{O}3$, $\text{O}6$, and $\text{O}7$ sites that can be O^{2-} or OH^- ions. The third group, which consists of $\text{O}8$ – $\text{O}10$ sites, has more than one short $\text{O}\cdots\text{O}$ contact, and therefore, only these sites can be H_2O molecules. Careful analysis found that only one of them ($\text{O}8$ – $\text{O}10$) can be an H_2O molecule. Assuming that $\text{O}8$ is an

H₂O molecule with two O–H groups directed toward O9 and O10 sites, O9 and O10 sites can contain only OH[−] or O^{2−} ions; otherwise, an unacceptably short distance between H atoms will be obtained. The same situation was found for the O9 and O10 sites, and thus, at most one H₂O molecule can exist in the asymmetric part of the unit cell. With this reasoning, two possible chemical formulas of NaLaW₂O₇(OH)₂(H₂O) and NaLaW₂O₆(OH)₄ remained.

To further identify the composition, we performed FTIR spectroscopy to reveal the functional groups built in the compound, and the results are shown in Figure 3. The sample

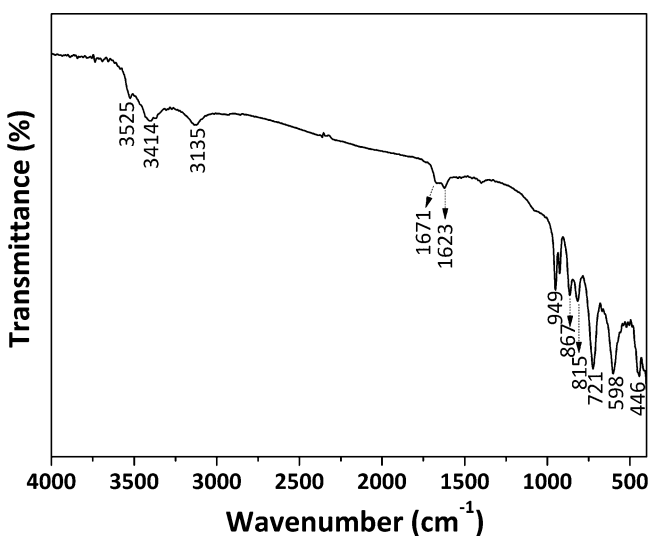


Figure 3. FTIR spectrum of NaLaW₂O₇(OH)₂(H₂O).

for FTIR analysis was dried in an air oven at 100 °C for 24 h to sufficiently evaporate surface-adsorbed water molecules, followed by immediate grinding with KBr granules (for IR absorptiometry, Wako Pure Chemicals, Osaka, Japan), pelleting, and analysis. It is evident from Figure 3 that the compound contains both hydroxyls (OH[−]) and hydration water, as evidenced by the vibrations at ~3525 cm^{−1}

(stretching mode of OH[−]), 3414 cm^{−1} (stretching mode of H₂O), and 1623 cm^{−1} (bending mode of H₂O). The additional absorptions occurring at ~3135 and 1671 cm^{−1} may arise from proton vibrations in O–H pairs. The multiplets in the spectral region of ~400–1000 cm^{−1} well correspond to the stretching, bending, and deformation modes of tungstate groups,^{44–47} though co-occurrence of the bending vibration of OH[−] (~600–1200 cm^{−1}) is also possible. With the help of FTIR, the compound under investigation was eventually assigned to be NaLaW₂O₇(OH)₂(H₂O). TG/DTA of the compound (Figure 4) revealed three stages of weight losses accompanied by endothermic effects up to ~350 °C. The first one (~0.45%) was ascribed to the evaporation of surface-adsorbed species, and the second and third (~3.83 and 1.40%, respectively) were related to dehydration and dehydroxylation. NaLaW₂O₇(OH)₂(H₂O) was calculated to have a theoretical weight loss of 5.18% upon being heated, which coincides with the sum of ~5.23% for the second and third stages of thermal decomposition revealed by TG.

The H atoms were not included in the final model, because numerous models will be generated by three probable H₂O molecule centers (Figure 2, right column) and four probable OH[−] group centers (Figure 2, middle column). Refinement of the decided model showed quite acceptable *R* factors (Table 1), and the resultant coordinates of atoms and main bond lengths are listed in Tables S1 and S2, respectively. The bond valence sums were calculated for all the heavy ions of La³⁺, W⁶⁺, and Na⁺ using constants from refs 48 and 49, and acceptable values within ±15% of real valences were obtained (Figure 5), which further supports the suggested structural model.

The crystal structure of NaLaW₂O₇(OH)₂(H₂O) is presented in Figure 6, and the unit cell viewed down the *a*-, *b*-, and *c*-axes can be found in Figure S1. The La³⁺ ion is coordinated by nine O sites forming three-capped trigonal prism (Figure 5). The LaO₉ polyhedra are linked with each other by sharing edges, forming a chain along the *b*-axis (Figure 6a). Two independent W sites were found in the asymmetric part of the unit cell, and each of them was coordinated by six O sites forming an octahedron (Figure 5).

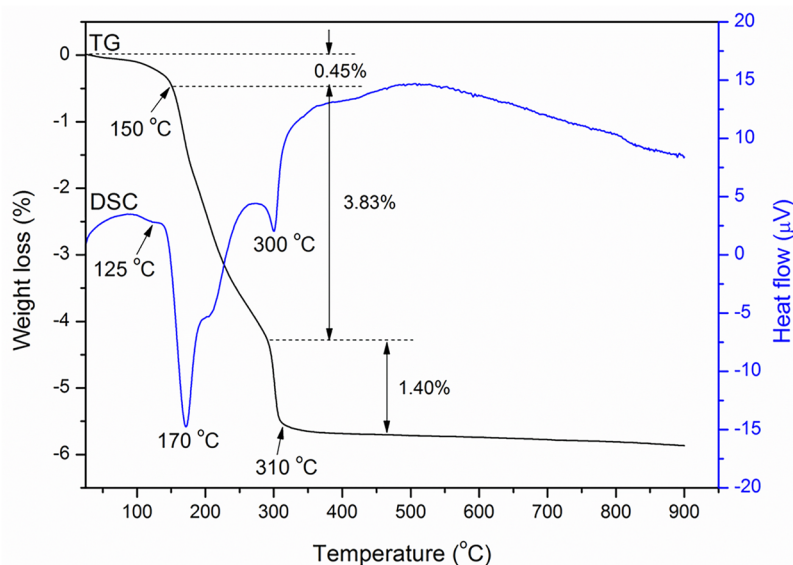
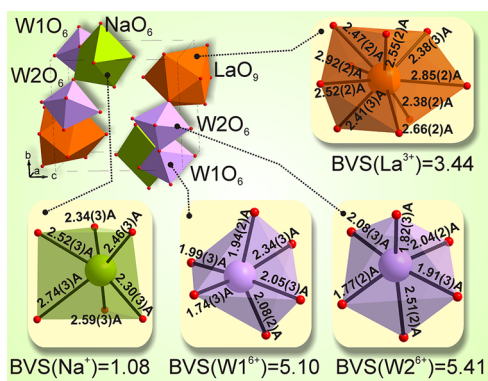


Figure 4. TG/DTA traces of NaLaW₂O₇(OH)₂(H₂O).

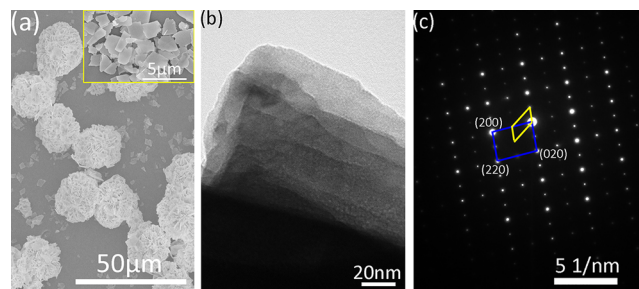
Table 1. Main Parameters of Processing and Results of Refinement for $\text{NaLaW}_2\text{O}_7(\text{OH})_2(\text{H}_2\text{O})$

space group	$P\bar{1}$
a (Å)	5.8671(2)
b (Å)	8.2440(2)
c (Å)	9.0108(3)
α (deg)	93.121(2)
β (deg)	75.280(2)
γ (deg)	94.379(2)
V (Å ³)	420.03(2)
Z	2
2θ interval (deg)	5–136.6
R_{wp} (%)	7.41
R_{p} (%)	5.33
R_{exp} (%)	2.30
χ^2	3.23
R_{B} (%)	2.33

**Figure 5.** Crystal structure of $\text{NaLaW}_2\text{O}_7(\text{OH})_2(\text{H}_2\text{O})$ without H atoms, together with the coordination of La^{3+} , W^{6+} , and Na^+ ions and the bond valence sums (BVS) calculated using bond lengths.

These octahedra are linked with each other by edge, forming a zigzag chain along the b -axis. The $-(\text{W1O}_6)-(\text{W1O}_6)-(\text{W2O}_6)-(\text{W2O}_6)-(\text{W1O}_6)-(\text{W1O}_6)-$ chains alternate with $-\text{LaO}_9-\text{LaO}_9-$ chains and join with each other by edges forming a two-dimensional (2D) layer in the $a-b$ plane (Figure 6a). The Na^+ ions are coordinated by six O sites forming NaO_6 trigonal prisms (Figure 5), which are linked with each other by edges (Figure 6b). The 2D layers in the $a-b$ plane are linked through NaO_6 prisms by edges to form a three-dimensional (3D) net (Figure 6b).

FE-SEM revealed that the $\text{NaLaW}_2\text{O}_7(\text{OH})_2(\text{H}_2\text{O})$ product mostly contains spheroids [$\sim 20\text{--}25\ \mu\text{m}$ in diameter (Figure 7a)] loosely agglomerated from microplate crystallites [thick-

**Figure 7.** (a) FE-SEM and (b) TEM morphologies and (c) SAED pattern of $\text{NaLaW}_2\text{O}_7(\text{OH})_2(\text{H}_2\text{O})$.

ness of $\sim 200\ \text{nm}$ (Figure S2a and the inset of Figure 7a)]. Doping of the RE^{3+} activator did not significantly change the overall morphology, as shown in Figure S2c for the $\text{Na}(\text{La}_{0.95}\text{Tb}_{0.05})\text{W}_2\text{O}_7(\text{OH})_2(\text{H}_2\text{O})$ representative. TEM analysis of the edge part of an individual microplate clearly reveals stacking of thin sheets (Figure 7b). Such a microstructural feature may well correspond to the 2D layers formed by $-(\text{W1O}_6)-(\text{W1O}_6)-(\text{W2O}_6)-(\text{W2O}_6)-(\text{W1O}_6)-(\text{W1O}_6)-$ and $-\text{LaO}_9-\text{LaO}_9-$ polyhedral chains alternating in the $a-b$ plane

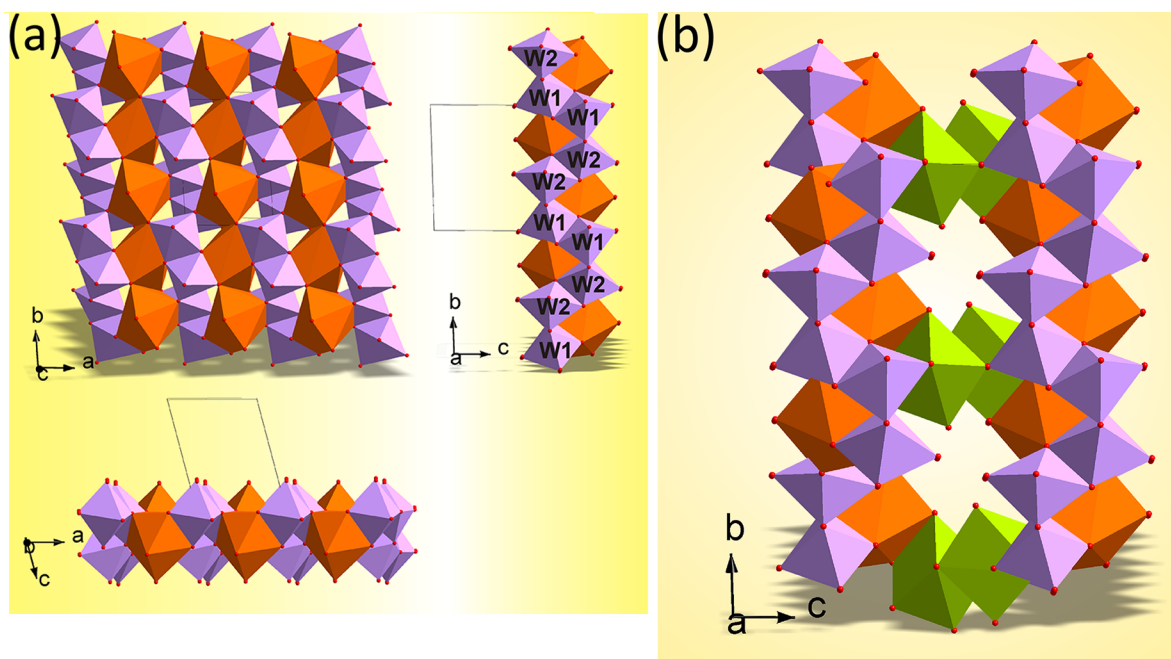
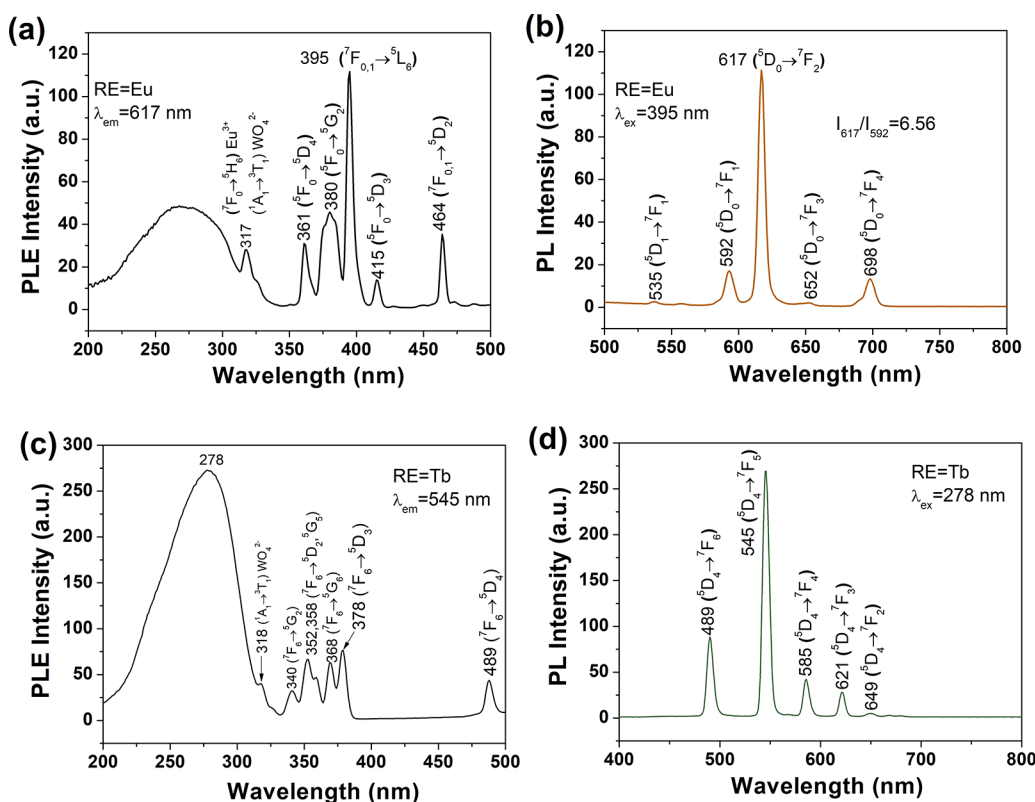
**Figure 6.** (a) Chain of $-(\text{W1O}_6)-(\text{W1O}_6)-(\text{W2O}_6)-(\text{W2O}_6)-(\text{W1O}_6)-(\text{W1O}_6)-$ polyhedra along the b -axis that alternates with the $-\text{LaO}_9-\text{LaO}_9-$ chain to form a 2D layer in the $a-b$ plane. (b) Two LaO_9-WO_6 layers are joined with each other through NaO_6 trigonal prisms.

Table 2. Unit Cell Parameters of the $\text{Na}(\text{La,RE})\text{W}_2\text{O}_7(\text{OH})_2(\text{H}_2\text{O})$ Crystals

	undoped	RE = Sm	RE = Eu	RE = Tb	RE = Dy
space group	$P\bar{1}$	$P\bar{1}$	$P\bar{1}$	$P\bar{1}$	$P\bar{1}$
<i>a</i> (Å)	5.8671(2)	5.8637(6)	5.8611(7)	5.8587(7)	5.8637(8)
<i>b</i> (Å)	8.2440(2)	8.2402(6)	8.2352(6)	8.2335(5)	8.2391(9)
<i>c</i> (Å)	9.0108(3)	9.0171(8)	9.0173(7)	9.0190(7)	9.0191(5)
α (deg)	93.121(2)	93.108(4)	93.104(7)	93.107(3)	93.107(9)
β (deg)	75.280(2)	75.284(8)	75.261(6)	75.283(5)	75.253(8)
γ (deg)	94.379(2)	94.350(5)	94.377(6)	94.373(5)	94.349(5)
<i>V</i> (Å ³)	420.03(2)	419.91(7)	419.42(8)	419.28(6)	419.89(8)

Figure 8. (a and c) PLE and (b and d) PL spectra of $\text{Na}(\text{La}_{0.95}\text{RE}_{0.05})\text{W}_2\text{O}_7(\text{OH})_2(\text{H}_2\text{O})$, where RE = Eu and Tb.

(Figure 6a). The selected area electron diffraction (SAED) pattern taken from the thin edge of the crystallite (Figure 7b) displays two sets of well-arranged spots (Figure 7c). The bright spots apparently originate from the *a*–*b* plane of the fundamental cell, and the measured *d* spacings of ~ 2.92 , 4.06 , and 2.30 Å (blue frame) can be assigned to the (200), (020), and (220) planes, respectively, of triclinic $\text{NaLaW}_2\text{O}_7(\text{OH})_2(\text{H}_2\text{O})$. The observed spacing values are close to the values of ~ 2.8313 , 4.1073 , and 2.2636 Å, respectively, derived via Rietveld refinement of the XRD pattern. The measured dihedral angles of $\sim 85.5^\circ$ and 51.4° for the (200)/(020) and (220)/(020) planes are also in good agreement with the values of $\sim 86.2^\circ$ and 52.9° obtained via Rietveld refinement, respectively. The results of TEM and Rietveld refinement that corresponded well further confirmed the crystal structure proposed for $\text{NaLaW}_2\text{O}_7(\text{OH})_2(\text{H}_2\text{O})$. The set of diffraction spots with weaker contrast in the SAED pattern (yellow frame) indicates the possible presence of sublattice structure,^{50–53} which can be caused by a slight deviation of atoms from their ideal positions.

3.2. Characterization and Luminescence of RE³⁺-Doped $\text{NaLaW}_2\text{O}_7(\text{OH})_2(\text{H}_2\text{O})$. As determined by XRD analysis (Figure S3), doping of $\text{NaLaW}_2\text{O}_7(\text{OH})_2(\text{H}_2\text{O})$ with the four types of practically important RE³⁺ activators of Eu³⁺ (5 atom %), Tb³⁺ (5 atom %), Sm³⁺ (2 atom %), and Dy³⁺ (2 atom %) did not alter the phase purity of the product. The lattice parameters and cell volumes of the $\text{Na}(\text{La,RE})\text{W}_2\text{O}_7(\text{OH})_2(\text{H}_2\text{O})$ solid solutions, which were obtained via Rietveld refinement of the XRD patterns (Figure S4), are summarized in Table 2. For the 9-fold coordination of rare-earth ions in this compound (Figure 5), La³⁺, Sm³⁺, Eu³⁺, Tb³⁺, and Dy³⁺ have ionic radii of 1.216, 1.132, 1.120, 1.095, and 1.083 Å, respectively.⁵⁴ In light of the rare-earth ions being solely located in the *a*–*b* plane of the crystal structure (Figure 6a), the substitution of larger La³⁺ with smaller RE³⁺ dopants could thus lead to smaller *a* and *b* constants. This provides direct evidence of the formation of the $\text{Na}(\text{La,RE})\text{W}_2\text{O}_7(\text{OH})_2(\text{H}_2\text{O})$ solid solution and is supported by the smaller cell volume of the doped sample. In particular, the Tb³⁺- and Dy³⁺-doped samples have *a* and *b* parameters and cell volumes that are smaller than those of the Eu³⁺- and Sm³⁺-

doped ones at the same doping level, which further confirmed the statement made above. The results of refinement also clearly indicated that shrinking the a - b plane expanded the unit cell along the c -axis, mostly through distortion of the NaO_6 trigonal prisms that connect the 2D layers constructed by $-(\text{W}_1\text{O}_6)-(\text{W}_1\text{O}_6)-(\text{W}_2\text{O}_6)-(\text{W}_2\text{O}_6)-(\text{W}_1\text{O}_6)-(\text{W}_1\text{O}_6)-$ and $-\text{LaO}_9-\text{LaO}_9-$ chains alternating in the a - b plane (Figure 6b).

$\text{Na}(\text{La},\text{RE})\text{W}_2\text{O}_7(\text{OH})_2(\text{H}_2\text{O})$ contains both hydroxyls and hydration water, which are known in the phosphor field to have a substantial quenching effect on RE^{3+} luminescence. Nevertheless, we investigated the photoluminescence of the four types of RE^{3+} activators and found that Eu^{3+} and Tb^{3+} are luminescent while Sm^{3+} and Dy^{3+} are essentially not in the visible light regime, as also found in the layered rare-earth hydroxides of $\text{RE}_2(\text{OH})_5\text{X}\cdot n\text{H}_2\text{O}$ ($\text{X} = \text{NO}_3^-$ or Cl^-).^{55–57} The negligibly weak Sm^{3+} and Dy^{3+} luminescence could be ascribed to the significantly abundant energy levels located between the lower-lying excited states and ground states of the two types of activators, which force the excitation energy to be readily dissipated via nonradiative relaxation, particularly in the mediation of hydration water and hydroxyls. Figure 8 shows the excitation and emission spectra of Eu^{3+} and Tb^{3+} in $\text{NaLaW}_2\text{O}_7(\text{OH})_2(\text{H}_2\text{O})$. For Eu^{3+} , the broad excitation band ($\lambda_{\text{em}} = 617$ nm) in the ~ 200 – 350 nm region [centered at ~ 270 nm (Figure 8a)] is known to overlap with excitation of the tungstate ligand ($^1\text{A}_{1g} \rightarrow \text{T}_{1u}/\text{T}_{1g}$ transition),^{58,59} which is dominant, and $\text{O}^{2-} \rightarrow \text{Eu}^{3+}$ charge transfer (CT), that is, excitation of electrons from the 2p orbital of O^{2-} to the 4f orbital of Eu^{3+} .⁶⁰ The occurrence of the former suggested the presence of energy transfer from tungstate ligands to Eu^{3+} activators. The shoulder peak at ~ 317 nm overlaps with the $^1\text{A}_1 \rightarrow ^3\text{T}_1$ and $^7\text{F}_0 \rightarrow ^5\text{H}_0$ excitations of the $[\text{WO}_4]^{2-}$ group and Eu^{3+} , respectively.²⁵ The sharp peaks in the longer wavelength region arise from electronic transitions within the $4f^6$ shell of Eu^{3+} , as labeled in the figure, with the $^7\text{F}_{0,1} \rightarrow ^5\text{L}_6$ excitation at ~ 395 nm dominating the whole excitation spectrum (Figure 8a). Tb^{3+} similarly presents two groups of excitation bands (Figure 8c), but the broad band in the short-UV region (~ 200 – 330 nm, centered at ~ 278 nm) overwhelms any of the intra- $4f^8$ excitation of Tb^{3+} in the ~ 330 – 500 nm region and is also significantly stronger than that found for the Eu^{3+} -doped sample. There are two main reasons for this phenomenon. One is the simultaneous occurrence of a $4f^8 \rightarrow 4f^7d^1$ interconfigurational Tb^{3+} transition (low-spin and high-spin), which is known to be prominent in various host lattices, and the other one is better matching of the emission of tungstate ligands and excitation energy levels of Tb^{3+} , as reported by Liu et al.⁶¹ and Liao et al.⁶² Under 395 and 278 nm excitations, the Eu^{3+} and Tb^{3+} activators exhibited their characteristic $^5\text{D}_{0,1} \rightarrow ^7\text{F}_j$ [$j = 1$ – 4 (Figure 8b)] and $^5\text{D}_4 \rightarrow ^7\text{F}_j$ [$j = 2$ – 6 (Figure 8d)] emission and have absolute quantum yields (η) of ~ 3.8 and 11.0% , respectively. The International de L'Éclairage (CIE) chromaticity coordinates were estimated from the luminescence spectra to be around (0.62, 0.37) for Eu^{3+} and (0.31, 0.58) for Tb^{3+} , which are typical of red and green colors (Figure S5), respectively. Because Eu^{3+} would reside at the noncentrosymmetric C_1 or C_s site in the triclinic lattice,⁶³ the $^5\text{D}_0 \rightarrow ^7\text{F}_2$ forced electric dipole transition (~ 617 nm) is remarkably stronger than the parity-allowed $^5\text{D}_0 \rightarrow ^7\text{F}_1$ magnetic dipole transition (~ 592 nm), with a $(^5\text{D}_0 \rightarrow ^7\text{F}_2)/(^5\text{D}_0 \rightarrow ^7\text{F}_1)$ intensity ratio (asymmetry factor; R) of ~ 6.56 . For Eu^{3+} , similar emission behaviors were observed in other

low-symmetry crystal structures, such as $\alpha\text{-Eu}_2(\text{MoO}_4)_3$,⁶⁴ $\text{CsGd}_{1-x}\text{Eu}_x(\text{MoO}_4)_2$,⁶⁵ and $\text{Rb}_3\text{EuB}_6\text{O}_{12}$.⁶⁶ For Tb^{3+} , green luminescence dominated by the ~ 545 nm band was widely observed for other hosts, such as $\beta\text{-Tb}_2(\text{MoO}_4)_3$ ⁶⁷ and $(\text{Gd},\text{Tb})_2\text{O}_3$.⁶⁸ The fluorescence decay kinetics were taken for the dominantly strong red emission of Eu^{3+} ($^5\text{D}_0 \rightarrow ^7\text{F}_2$ transition, ~ 617 nm; $\lambda_{\text{ex}} = 395$ nm) and green emission of Tb^{3+} ($^5\text{D}_4 \rightarrow ^7\text{F}_5$ transition, ~ 545 nm; $\lambda_{\text{ex}} = 278$ nm). It was found that the decay data can be fit well with the single-exponential equation $I = A \exp(-t/\tau) + B$, where τ , t , and I denote the fluorescence lifetime, delay time, and instantaneous emission intensity, respectively, and A and B are constants. The results of fitting (Figure S6) yielded fluorescence lifetimes of ~ 1.19 ms for Eu^{3+} and 1.38 ms for Tb^{3+} . The major luminescent properties of these two samples are summarized in Table 3.

Table 3. Summary of Photoluminescence Properties for $\text{Na}(\text{La}_{0.95}\text{RE}_{0.05})\text{W}_2\text{O}_7(\text{OH})_2(\text{H}_2\text{O})$

RE type	λ_{ex} (nm)	λ_{em} (nm)	CIE coordinates	color	lifetime (ms)	η (%)	R
Eu	395	617	(0.62, 0.37)	red	1.19	3.8	6.56
Tb	278	545	(0.31, 0.58)	green	1.38	11.0	–

3.3. Characterization and Photoluminescence of the Calcination-Derived $\text{Na}(\text{La},\text{RE})(\text{WO}_4)_2$ Double Tungstate ($\text{RE} = \text{Sm}, \text{Eu}, \text{Tb}$, and Dy). $\text{NaLaW}_2\text{O}_7(\text{OH})_2(\text{H}_2\text{O})$ would decompose to $\text{NaLa}(\text{WO}_4)_2$ at the very low temperature of ~ 350 °C, as suggested by the results of TG/DTA (Figure 4). For sufficient dehydration and hydroxylation, however, the $\text{Na}(\text{La},\text{RE})(\text{WO}_4)_2$ phosphors were obtained in this work by calcining their respective precursors at the higher temperature of 500 °C. Figure 9 exhibits XRD patterns of the calcination

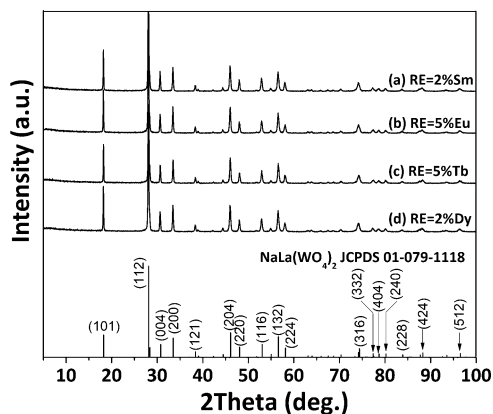


Figure 9. XRD patterns of the $\text{Na}(\text{La},\text{RE})(\text{WO}_4)_2$ phosphors calcined from their respective hydrothermal precursors at 500 °C. The standard diffractions of $\text{NaLa}(\text{WO}_4)_2$ (JCPDS Card No. 01-079-1118)⁶⁹ are included as bars for comparison.

products, where it is seen that the diffraction peaks can be fully indexed with tetragonally structured $\text{NaLa}(\text{WO}_4)_2$ (JCPDS Card No. 01-079-1118,⁶⁹ space group $I4_1/a$) in each case. The observation of morphology shows that the loose agglomerates in the precursor were mostly disintegrated into individual microplates, possibly because of the release of water vapor during calcination (Figure S2b,d). The results of Rietveld fitting of the XRD patterns are shown in Figure S7 and Table S3. It is seen that RE^{3+} doping shrunk a ($a = b$) and c

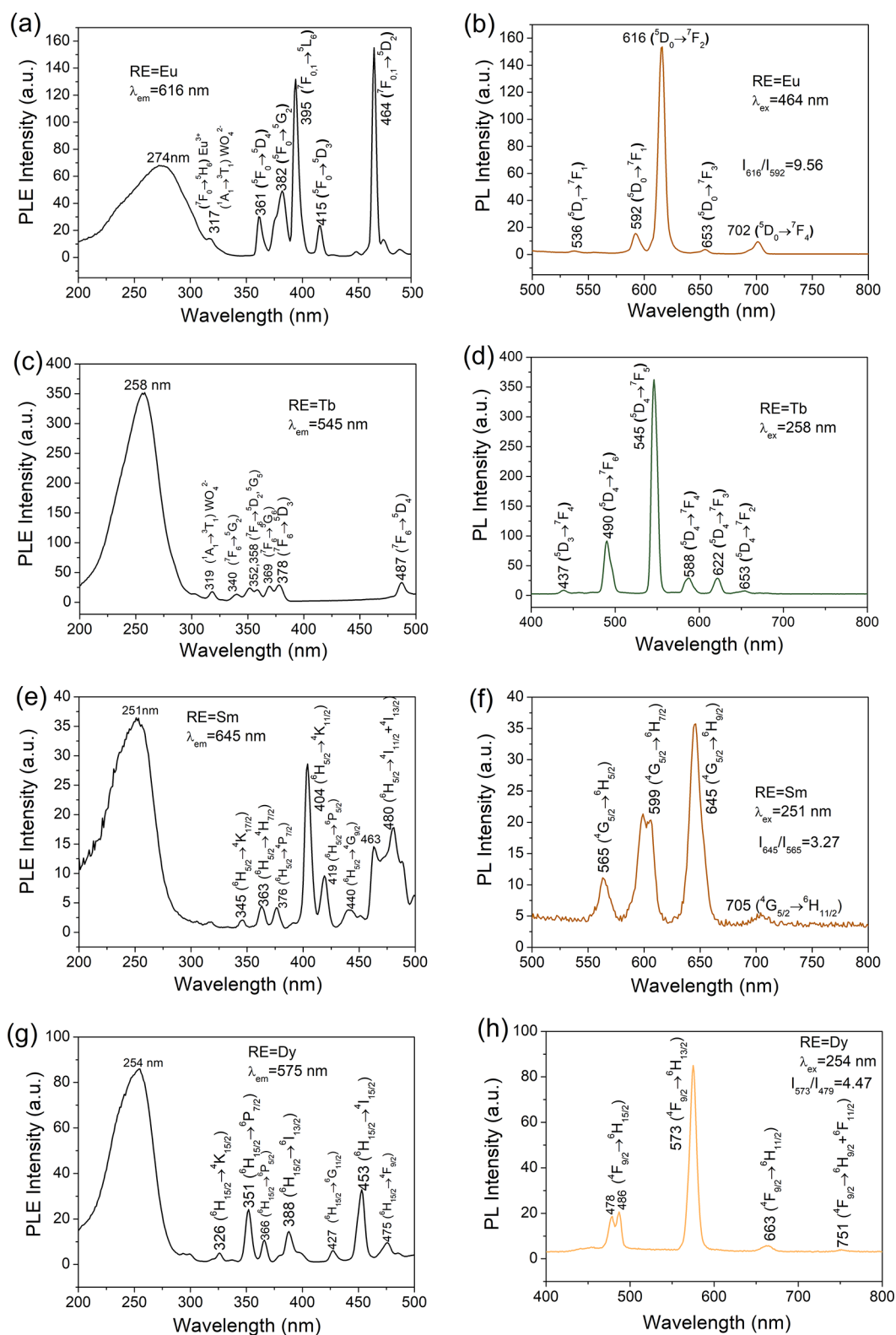


Figure 10. PLE (left column) and PL (right column) spectra for the $\text{Na}(\text{La,RE})(\text{WO}_4)_2$ phosphors, where RE = Eu (a and b), Tb (c and d), Sm (e and f), and Dy (g and h).

parameters and cell volume V of the crystal structure, and the product of a smaller RE^{3+} has smaller cell dimensions and a smaller cell volume at the same RE^{3+} content (Table S3). That is, the results suggested the formation of $\text{Na}(\text{La,RE})(\text{WO}_4)_2$ solid solutions.

Figure 10 exhibits PLE and PL spectra of the $\text{Na}(\text{La,RE})(\text{WO}_4)_2$ phosphors. A common feature of the PLE spectra is that they are composed of a broad band in the short-UV region (roughly 200–300 nm, group I) and a series of sharp peaks in the ~300–500 nm region (group II), similar to those shown in Figure 8. As discussed above, the group I bands overlap with

tungstate excitation (promotion of electrons from the 2p orbital of O^{2-} to the 5d orbital of W^{6+} within the tungstate ligand; $O^{2-} \rightarrow W^{6+}$ CT)^{58,59,70} and $O^{2-} \rightarrow RE^{3+}$ CT (RE = Eu, Sm, and Dy) or $4f^8 \rightarrow 4f^7d^1$ interconfigurational transition (RE = Tb), while the group II bands arise from intra-4f⁵ (Sm^{3+}), -4f⁶ (Eu^{3+}), -4f⁸ (Tb^{3+}), and -4f⁹ (Dy^{3+}) excitation transitions, as specified in the corresponding parts of Figure 10. The peak position and broadness of group I bands are largely related to two factors, that is, the separation distance between $O^{2-} \rightarrow W^{6+}$ CT and $O^{2-} \rightarrow RE^{3+}$ CT ($f \rightarrow d$ transition for Tb) and the extent of crystal field splitting of the 5d energy level of W^{6+} , with the latter being substantially affected by the lattice covalency, the W–O bond length, and the geometry and distortion of [W–O] polyhedra. These may account for the apparently broader feature of the group I band of Eu^{3+} and narrowing toward the shorter-UV region of the group I bands of Eu^{3+} and Tb^{3+} in $NaLa(WO_4)_2$ compared to that in $NaLaW_2O_7(OH)_2(H_2O)$. A comparison of Figures 8a and 10a revealed that, unlike in $NaLaW_2O_7(OH)_2(H_2O)$, Eu^{3+} shows stronger ${}^7F_{0,1} \rightarrow {}^5D_2$ (~465 nm) than ${}^7F_{0,1} \rightarrow {}^5L_6$ (~395 nm) excitation in $NaLa(WO_4)_2$, as also observed by Liu et al.⁵ and Wang et al.⁷¹ Though the exact reason needs to be clarified, the phenomenon may suggest that the electrons excited to the 5L_6 level of Eu^{3+} seem to have more interactions with the CT states of W^{6+} and Eu^{3+} . It is also noteworthy that, except for Eu^{3+} , the excitation spectra are dominated by group I bands in each case. This implies that the emission spectrum of tungstate ligands matches better with the excitation spectra of Tb^{3+} , Sm^{3+} , and Dy^{3+} , and as a consequence, more efficient energy transfer from excited $[WO_4]^{2-}$ ligands to activators takes place.^{61,62} Through excitement with the peak wavelength of the strongest excitation band, the phosphors present dominantly strong red (Eu^{3+} , ~616 nm), green (Tb^{3+} , ~545 nm), deep red (Sm^{3+} , ~645 nm), and yellow (Dy^{3+} , ~573 nm) emission. $NaLa(WO_4)_2$ crystallizes in the sheelite-type tetragonal structure, which consists of $[WO_4]$ tetrahedra and $[NaO_8]$ and $[LaO_8]$ polyhedra, with the La^{3+} ions connected via La–O–W–O–La.⁷¹ Though La^{3+} was expected to have D_{3d} theoretical site symmetry in such a crystal structure, the statistical distribution of Na^+/La^{3+} ions lowers centrosymmetric D_{3d} to noncentrosymmetric C_2 symmetry in practice.⁷¹ For this, the parity-forbidden electric dipole transitions of ${}^5D_0 \rightarrow {}^7F_2$ (~616 nm), ${}^4G_{5/2} \rightarrow {}^6H_{9/2}$ (~645 nm), and ${}^4F_{9/2} \rightarrow {}^6H_{13/2}$ (~573 nm) appear stronger than the parity-allowed magnetic dipole transitions of ${}^5D_0 \rightarrow {}^7F_1$ (~592 nm), ${}^4G_{5/2} \rightarrow {}^6H_{5/2}$ (~565 nm), and ${}^4F_{9/2} \rightarrow {}^6H_{15/2}$ (~480 nm) for Eu^{3+} , Sm^{3+} , and Dy^{3+} , respectively.

The electronic transitions that are responsible for the observed emission bands are assigned in the corresponding parts of Figure 10, and the luminescence properties of the four phosphors are summarized in Table 4, including dominant excitation (λ_{ex}) and emission (λ_{em}) wavelengths, quantum efficiencies (η) of luminescence, CIE color coordinates, emission colors (Figure S8), fluorescence lifetimes derived via single-exponential fitting of the decay curve (Figure S9), and asymmetry factors of luminescence (R , intensity ratio of forced electric dipole transition to magnetic dipole transition). It is seen that $NaLa(WO_4)_2$ presents higher quantum efficiencies and longer lifetimes compared to those of $NaLaW_2O_7(OH)_2(H_2O)$ for Eu^{3+} and Tb^{3+} luminescence.

Table 4. Photoluminescence Properties for $Na(La,RE)(WO_4)_2$

RE type	λ_{ex} (nm)	λ_{em} (nm)	CIE coordinates	color	lifetime (ms)	η (%)	R
Eu	464	615	(0.58, 0.41)	red	1.60	4.5	9.56
Tb	258	545	(0.31, 0.51)	green	1.48	15.3	–
Sm	251	645	(0.56, 0.43)	red	1.73	5.9	3.27
Dy	254	575	(0.39, 0.42)	yellow	1.33	5.2	4.47

4. CONCLUSIONS

Hydrothermally reacting $La(NO_3)_3$ and $Na_2WO_4 \cdot 2H_2O$ at 100 °C and pH 8 yielded the new compound $NaLaW_2O_7(OH)_2(H_2O)$, which dehydrates to $NaLa(WO_4)_2$ up to ~350 °C. Doping the two types of double tungstates with practically important Eu^{3+} , Tb^{3+} , Sm^{3+} , and Dy^{3+} activators to form solid solutions was also achieved. Detailed analysis of the compounds in terms of structure and photoluminescence led to the following main conclusions.

(1) $NaLaW_2O_7(OH)_2(H_2O)$ crystallizes in the triclinic system (space group $P\bar{1}$), with lattice constants $a = 5.8671(2)$ Å, $b = 8.2440(2)$ Å, and $c = 9.0108(3)$ Å, axis angles $\alpha = 93.121(2)^\circ$, $\beta = 75.280(2)^\circ$, and $\gamma = 94.379(2)^\circ$, and cell volume $V = 420.03(2)$ Å³. The crystal structure contains 2D layers of $-(W1O_6)-(W1O_6)-(W2O_6)-(W2O_6)-(W1O_6)-(W1O_6)-$ and $-LaO_9-LaO_9-$ chains alternating in the $a-b$ plane, which are linked together through NaO_6 octahedral trigonal prisms by edges to form a 3D net.

(2) Only Eu^{3+} and Tb^{3+} are favorably luminescent in $Na(La,RE)W_2O_7(OH)_2(H_2O)$, whose main excitation/emission wavelengths, quantum yields, and fluorescence lifetimes are 395/617 and 278/545 nm, ~3.8 and 11.0%, and ~1.19 and 1.38 ms, respectively.

(3) $Na(La,RE)(WO_4)_2$ exhibits dominantly strong red (~616 nm for Eu^{3+} ; $\lambda_{ex} = 464$ nm), green (545 nm for Tb^{3+} ; $\lambda_{ex} = 258$ nm), deep red (~645 nm for Sm^{3+} ; $\lambda_{ex} = 251$ nm), and yellow (~573 nm for Dy^{3+} ; $\lambda_{ex} = 254$ nm) emission. The quantum yield of luminescence and the fluorescence lifetime of the main emission are ~4.5% and 1.60 ms for Eu^{3+} , 15.3% and 1.48 ms for Tb^{3+} , 5.9% and 1.73 ms for Sm^{3+} , and 5.2% and 1.33 ms for Dy^{3+} , respectively.

■ ASSOCIATED CONTENT

Supporting Information

The Supporting Information is available free of charge on the ACS Publications website at DOI: 10.1021/acs.inorgchem.8b02228.

Fractional atomic coordinates, isotropic displacement parameters, and main bond lengths of $NaLaW_2O_7(OH)_2(H_2O)$; FE-SEM images of $NaLaW_2O_7(OH)_2(H_2O)$ and $NaLa(WO_4)_2$ and their Tb^{3+} -doped counterparts; Rietveld refinement of XRD patterns, CIE chromaticity diagrams, and fluorescence decay curves for $Na(La,RE)W_2O_7(OH)_2(H_2O)$ and $Na(La,RE)(WO_4)_2$; and structural parameters of $Na(La,RE)(WO_4)_2$ (PDF)

Accession Codes

CCDC 1860433 contains the supplementary crystallographic data for this paper. These data can be obtained free of charge

via www.ccdc.cam.ac.uk/data_request/cif, or by emailing data_request@ccdc.cam.ac.uk, or by contacting The Cambridge Crystallographic Data Centre, 12 Union Road, Cambridge CB2 1EZ, UK; fax: +44 1223 336033.

AUTHOR INFORMATION

Corresponding Authors

*Telephone: +81-29-860-4394. E-mail: li.jiguang@nims.go.jp.

*Telephone: +7-391-249-4507. E-mail: msmolokeev@gmail.com.

ORCID

Xuejiao Wang: 0000-0003-4327-2340

Xiaofei Shi: 0000-0001-6934-5427

Qi Zhu: 0000-0001-5513-6309

Ji-Guang Li: 0000-0002-5625-7361

Notes

The authors declare no competing financial interest.

ACKNOWLEDGMENTS

This work is supported in part by the National Natural Science Foundation of China (Grants 51702020 and 51672039), the Doctoral Research Fund of Liaoning Province (Grant 20170520103), and RFBR via Research Project 17-52-53031.

REFERENCES

- (1) Yu, X. C.; Gao, M. L.; Li, J. X.; Duan, L.; Cao, N.; Jiang, Z. Q.; Hao, A. B.; Zhao, P.; Fan, J. B. Near infrared to visible upconversion emission in $\text{Er}^{3+}/\text{Yb}^{3+}$ co-doped $\text{NaGd}(\text{WO}_4)_2$ nanoparticles obtained by hydrothermal method. *J. Lumin.* **2014**, *154*, 111–115.
- (2) Mateos, X.; Pujol, M. C.; Güell, F.; Galán, M.; Solé, R. M.; Gavalda, J.; Aguiló, M.; Massons, J.; Diaz, F. Erbium spectroscopy and 1.5- μm emission in $\text{KGd}(\text{WO}_4)_2$: Er , Yb single crystals. *IEEE J. Quantum Electron.* **2004**, *40*, 759–770.
- (3) Subbotin, K. A.; Zharikov, E. V.; Smirnov, V. A. Yb- and Er-doped single crystals of double tungstates $\text{NaGd}(\text{WO}_4)_2$, $\text{NaLa}(\text{WO}_4)_2$, and $\text{NaBi}(\text{WO}_4)_2$ as active media for lasers operating in the 1.0 and 1.5 μm ranges. *Opt. Spectrosc.* **2002**, *92*, 601–608.
- (4) Huang, J. H.; Gong, X. H.; Chen, Y. J.; Lin, Y. F.; Liao, J. S.; Chen, X. Y.; Luo, Z. D.; Huang, Y. D. Polarized spectral properties of Er^{3+} ions in $\text{NaGd}(\text{WO}_4)_2$ crystal. *Appl. Phys. B: Lasers Opt.* **2007**, *89*, 73–80.
- (5) Liu, X. L.; Hou, W. H.; Yang, X. Y.; Liang, J. Y. Morphology controllable synthesis of $\text{NaLa}(\text{WO}_4)_2$: the morphology dependent photoluminescent properties and single-phased white light emission of $\text{NaLa}(\text{WO}_4)_2$: $\text{Eu}^{3+}/\text{Tb}^{3+}/\text{Tm}^{3+}$. *CrystEngComm* **2014**, *16*, 1268–1276.
- (6) Sun, C.; Yang, F.; Tu, C. Spectroscopic properties of $\text{Tm}^{3+}/\text{Ho}^{3+}$ co-doped $\text{NaLa}(\text{WO}_4)_2$ single crystal. *J. Lumin.* **2012**, *132*, 1232–1236.
- (7) Atuchin, V. V.; Kesler, V. G.; Maklakova, N. Y.; Pokrovsky, L. D. Core level spectroscopy and RHEED analysis of $\text{KGd}(\text{WO}_4)_2$ Surface. *Solid State Commun.* **2005**, *133*, 347–351.
- (8) Atuchin, V. V.; Kesler, V. G.; Maklakova, N. Y.; Pokrovsky, L. D.; Sheglov, D. V. Core level spectroscopy and RHEED analysis of $\text{KGd}_{0.95}\text{Nd}_{0.05}(\text{WO}_4)_2$ surface. *Eur. Phys. J. B* **2006**, *51*, 293–300.
- (9) Ropuszńska-Robak, P.; Tomaszewski, P. E.; Kepínski, L.; Macalik, L. Alkali metal impact on structural and phonon properties of Er^{3+} and Tm^{3+} co-doped $\text{MY}(\text{WO}_4)_2$ ($M = \text{Li}, \text{Na}, \text{K}$) nanocrystals. *RSC Adv.* **2018**, *8*, 2632–2641.
- (10) Liu, Y.; Liu, Y. X.; Liu, G. X.; Dong, X. T.; Wang, J. X. Up/down conversion, tunable photoluminescence and energy transfer properties of $\text{NaLa}(\text{WO}_4)_2$: $\text{Er}^{3+}, \text{Eu}^{3+}$ phosphors. *RSC Adv.* **2015**, *5*, 97995–98003.

- (11) Rasu, K. K.; Balaji, D.; Babu, S. M. Spectroscopic properties of Eu^{3+} : $\text{KLa}(\text{WO}_4)_2$ novel red phosphors. *J. Lumin.* **2016**, *170*, 547–555.

- (12) Zhang, Y.; Gong, W. T.; Yu, J. J.; Cheng, Z. Y.; Ning, G. L. Multicolor luminescence properties and energy transfer behavior in host-sensitized CaWO_4 : Tb^{3+} , Eu^{3+} phosphors. *RSC Adv.* **2016**, *6*, 30886–30894.

- (13) Kaminskii, A. A. *Laser Crystal*; Springer: Berlin, 1981; p 111.

- (14) Guo, T.; Lin, Y.; Zhang, W.-J.; Hong, J.-S.; Lin, R.-H.; Wu, X.-P.; Li, J.; Lu, C.-H.; Yang, H.-H. High-efficiency X-ray luminescence in Eu^{3+} -activated tungstate nanoprobles for optical imaging through energy transfer sensitization. *Nanoscale* **2018**, *10*, 1607–1612.

- (15) Laguna, M.; Escudero, A.; Núñez, N. O.; Becerro, A. I.; Ocaña, M. Europium-doped $\text{NaGd}(\text{WO}_4)_2$ nanophosphors: synthesis, luminescence and their coating with fluorescein for pH sensing. *Dalton Trans* **2017**, *46*, 11575–11583.

- (16) Xu, S.; Xiang, S. Y.; Zhang, Y. Q.; Zhang, J. S.; Li, X. P.; Sun, J. S.; Cheng, L. H.; Chen, B. J. 808 nm laser induced photothermal effect on $\text{Sm}^{3+}/\text{Nd}^{3+}$ doped $\text{NaY}(\text{WO}_4)_2$ microstructures. *Sens. Actuators, B* **2017**, *240*, 386–391.

- (17) Huang, S. Q.; Lou, Z. Y.; Qi, Z. B.; Zhu, N. W.; Yuan, H. P. Enhancing upconversion emissions of $\text{Er}^{3+}/\text{Tm}^{3+}/\text{Yb}^{3+}$ tridoped ($\text{NaY}(\text{WO}_4)_2/\text{YF}_3$) through TiO_2 coating and Bi^{3+} doping and its photocatalytic applications. *Appl. Catal., B* **2015**, *168–169*, 313–321.

- (18) Xiong, F. B.; Zhang, Z. W.; Lin, H. F.; Wang, L. J.; Xu, Y. C.; Zhu, W. Z. Luminescent properties of deep red light-emitting phosphors $\text{NaGd}(\text{WO}_4)_2$: Pr^{3+} for blue LED. *Opt. Mater.* **2015**, *42*, 394–398.

- (19) Zheng, H.; Chen, B. J.; Yu, H. Q.; Zhang, J. S.; Sun, J. S.; Li, X. P.; Sun, M.; Tian, B. N.; Fu, S. B.; Zhong, H.; Dong, B.; Hua, R. N.; Xia, H. P. Microwave-assisted hydrothermal synthesis and temperature sensing application of $\text{Er}^{3+}/\text{Yb}^{3+}$ doped $\text{NaY}(\text{WO}_4)_2$ microstructures. *J. Colloid Interface Sci.* **2014**, *420*, 27–34.

- (20) Lei, F.; Huang, L. J.; Shi, Y.; Xie, J. J.; Zhang, L.; Xiao, W. Q. Molten salt synthesis of color-tunable and single-component $\text{NaY}_{(1-x-y)}(\text{WO}_4)_2$: $\text{Eu}^{3+}_x\text{Tb}^{3+}_y$ phosphor for UV LEDs. *J. Mater. Res.* **2017**, *32*, 1548–1554.

- (21) Yang, Y.; Feng, H.; Zhang, X. G. Microwave heating synthesis and luminescence of $\text{NaY}(\text{WO}_4)_2$: (Ho^{3+} , Yb^{3+}) phosphors. *J. Mater. Sci.: Mater. Electron.* **2015**, *26*, 229–233.

- (22) Lim, C. S. Microwave-modified sol-gel process of $\text{NaY}(\text{WO}_4)_2$: $\text{Ho}^{3+}/\text{Yb}^{3+}$ phosphors and the upconversion of their photoluminescence properties. *Ceram. Int.* **2015**, *41*, 2616–2621.

- (23) Tan, X.; Wang, Y. R.; Zhang, M. Y. Solvothermal synthesis, luminescence and energy transfer of Dy^{3+} and Sm^{3+} doped $\text{NaLa}(\text{WO}_4)_2$ nanocubes. *J. Photochem. Photobiol., A* **2018**, *353*, 65–70.

- (24) Kaczmarek, A. M.; van Deun, R. Rare earth tungstate and molybdate compounds - from 0D to 3D architectures. *Chem. Soc. Rev.* **2013**, *42*, 8835–8848.

- (25) Shi, X. F.; Li, J.-G.; Wang, X. J.; Zhu, Q.; Kim, B.-N.; Sun, X. D. Facile hydrothermal crystallization of $\text{NaLn}(\text{WO}_4)_2$ ($\text{Ln} = \text{La}, \text{Lu}$, and Y), phase/morphology evolution, and photoluminescence. *Sci. Technol. Adv. Mater.* **2017**, *18*, 741–754.

- (26) Wesolowski, D.; Drummond, S. E.; Mesmer, R. E.; Ohmoto, H. Hydrolysis Equilibria of Tungsten(VI) in Aqueous Sodium Chloride Solutions to 300 °C. *Inorg. Chem.* **1984**, *23*, 1120–1132.

- (27) Shi, X. F.; Wang, Z. H.; Takei, T.; Wang, X. J.; Zhu, Q.; Li, X. D.; Kim, B.-N.; Sun, X. D.; Li, J.-G. Selective Crystallization of Four Tungstates ($\text{La}_2\text{W}_3\text{O}_{12}$, $\text{La}_2\text{W}_2\text{O}_9$, $\text{La}_{14}\text{W}_8\text{O}_{45}$, and $\text{La}_6\text{W}_2\text{O}_{15}$) via Hydrothermal Reaction and Comparative Study of Eu^{3+} Luminescence. *Inorg. Chem.* **2018**, *57*, 6632–6640.

- (28) Torres, J.; Tissot, F.; Santos, P.; Ferrari, C.; Kremer, C.; Kremer, E. Interactions of W(VI) and Mo(VI) Oxyanions with Metal Cations in Natural Waters. *J. Solution Chem.* **2016**, *45*, 1598–1611.

- (29) Davantès, A.; Costa, D.; Lefèvre, G. Infrared Study of (Poly)tungstate Ions in Solution and Sorbed into Layered Double Hydroxides: Vibrational Calculations and In Situ Analysis. *J. Phys. Chem. C* **2015**, *119*, 12356–12364.

- (30) May, P. M.; Murray, K. JESS, A Joint Expert Speciation System-I. Raison d'être. *Talanta* **1991**, *38*, 1409–1417.
- (31) Aveston, J. Hydrolysis of Tungsten(VI): Ultracentrifugation, Acidity Measurements, and Raman Spectra of Polytungstates. *Inorg. Chem.* **1964**, *3*, 981–986.
- (32) Koutsospyros, A.; Braida, W.; Christodoulatos, C.; Dermatas, D.; Strigul, N. A Review of Tungsten: from Environmental Obscurity to Scrutiny. *J. Hazard. Mater.* **2006**, *136*, 1–19.
- (33) Rozantsev, G. M.; Sazonova, O. I. Thermodynamic Parameters of Interconversions of Isopolyanions in Solutions of Tungsten(VI). *Russ. J. Coord. Chem.* **2005**, *31*, 552–558.
- (34) Pettit, L. D.; Powell, K. J. The IUPAC Stability Constants Database. *Chem. Int.* **2006**, *28*, 14–15.
- (35) Cruywagen, J. J. Protonation, Oligomerization and Condensation Reactions of Vanadate(V), Molybdate(VI) and Tungstate(VI). *Adv. Inorg. Chem.* **1999**, *49*, 127–182.
- (36) Thompson, L. C. Complexes. In *Handbook on the Physics and Chemistry of Rare Earths*; Gschneidner, K. A., Jr., Eyring, L., Eds.; North-Holland Physics: Amsterdam, 1979.
- (37) Rizkalla, E. N.; Choppin, G. R. Hydration of lanthanides and actinides in solution. *J. Alloys Compd.* **1992**, *180*, 325–336.
- (38) Kaczmarek, A. M.; Van Hecke, K.; Van Deun, R. Enhanced Luminescence in Ln³⁺-doped Y₂WO₆ (Sm, Eu, Dy) 3D Microstructures through Gd³⁺ Codoping. *Inorg. Chem.* **2014**, *53*, 9498–9508.
- (39) Byrappa, K.; Jain, A. Hydrothermal Growth and Characterization of NaLa(WO₄)₂ Crystals. *J. Mater. Res.* **1996**, *11*, 2869–2875.
- (40) Liu, Y.; Liu, G. X.; Wang, J. X.; Dong, X. T.; Yu, W. S. Single-Component and Warm-White-Emitting Phosphor NaGd(WO₄)₂:Tm³⁺, Dy³⁺, Eu³⁺: Synthesis, Luminescence, Energy Transfer, and Tunable Color. *Inorg. Chem.* **2014**, *53*, 11457–11466.
- (41) Wang, J. Y.; Zhang, C. M.; Liu, Y. M.; Li, L. F.; Liu, S.; Jia, G.; Shen, S. G. Well-defined sodium lanthanum tungstate hierarchical microcrystals: Controllable synthesis and luminescence properties. *J. Alloys Compd.* **2015**, *633*, 395–400.
- (42) TOPAS V4.2: General profile and structure analysis software for powder diffraction data - User's Manual; Bruker AXS: Karlsruhe, Germany, 2008.
- (43) Favre-Nicolin, V.; Černý, R. FOX 'free objects for crystallography': a modular approach to ab initio structure determination from powder diffraction. *J. Appl. Crystallogr.* **2002**, *35*, 734–743.
- (44) Gadsden, J. A. *Infrared spectra of minerals and related inorganic compounds*; Butterworth: Newton, MA, 1975.
- (45) Alekseev, E. V.; Felbinger, O.; Wu, S.; Malcherek, T.; Depmeier, W.; Modolo, G.; Gesing, T. M.; Krivovichev, S. V.; Suleimanov, E. V.; Gavrilova, T. A.; Pokrovsky, L. D.; Pugachev, A. M.; Surovtsev, N. V.; Atuchin, V. V. K[AsW₂O₉], the first member of the arsenate-tungsten bronze family: Synthesis, structure, spectroscopic and non-linear optical properties. *J. Solid State Chem.* **2013**, *204*, 59–63.
- (46) Zhao, P.; Murshed, M. M.; Alekseev, E. V.; Atuchin, V. V.; Pugachev, A. M.; Gesing, T. M. Synthesis, structure and properties of Na[AsW₂O₉]. *Mater. Res. Bull.* **2014**, *60*, 258–263.
- (47) Lim, C. S.; Aleksandrovsky, A.; Molokeev, M. S.; Oreshonkov, A.; Atuchin, V. V. Microwave sol-gel synthesis and upconversion photoluminescence properties of CaGd₂(WO₄)₄:Er³⁺/Yb³⁺ phosphors with incommensurately modulated structure. *J. Solid State Chem.* **2015**, *228*, 160–166.
- (48) Brown, I. D.; Altermatt, D. Bond-valence parameters obtained from a systematic analysis of the Inorganic Crystal Structure Database. *Acta Crystallogr., Sect. B: Struct. Sci.* **1985**, *41*, 244–247.
- (49) Trzesowska, A.; Kruzynski, R.; Bartczak, T. J. New bond-valence parameters for lanthanides. *Acta Crystallogr., Sect. B: Struct. Sci.* **2004**, *60*, 174–178.
- (50) Geng, F. X.; Xin, H.; Matsushita, Y.; Ma, R. Z.; Tanaka, M.; Izumi, F.; Iyi, N.; Sasaki, T. New Layered Rare-Earth Hydroxides with Anion-Exchange Properties. *Chem. - Eur. J.* **2008**, *14*, 9255–9260.
- (51) Abakumov, A. M.; Morozov, V. A.; Tsirlin, A. A.; Verbeeck, J.; Hadermann, J. Cation Ordering and Flexibility of the BO₄²⁻ Tetrahedra in Incommensurately Modulated CaEu₂(BO₄)₄ (B = Mo, W) Scheelites. *Inorg. Chem.* **2014**, *53*, 9407–9415.
- (52) Lim, C. S.; Aleksandrovsky, A.; Molokeev, M. S.; Oreshonkov, A.; Atuchin, V. V. The modulated structure and frequency upconversion properties of CaLa₂(MoO₄)₄:Ho³⁺/Yb³⁺ phosphors prepared by microwave synthesis. *Phys. Chem. Chem. Phys.* **2015**, *17*, 19278–19287.
- (53) Lim, C. S.; Atuchin, V. V.; Aleksandrovsky, A. S.; Molokeev, M. S.; Oreshonkov, A. S. Incommensurately modulated structure and spectroscopic properties of CaGd₂(MoO₄)₄:Ho³⁺/Yb³⁺ phosphors for up-conversion applications. *J. Alloys Compd.* **2017**, *695*, 737–746.
- (54) Shannon, R. D. Revised effective ionic radii and systematic studies of interatomic distances in halides and chalcogenides. *Acta Crystallogr., Sect. A: Cryst. Phys., Diffr., Theor. Gen. Crystallogr.* **1976**, *32*, 751–767.
- (55) Wu, X. L.; Li, J.-G.; Zhu, Q.; Liu, W. G.; Li, J.; Li, X. D.; Sun, X. D.; Sakka, Y. One-step freezing temperature crystallization of layered rare-earth hydroxide (Ln₂(OH)₅NO₃·nH₂O) nanosheets for a wide spectrum of Ln (Ln = Pr–Er, and Y), anion exchange with fluorine and sulfate, and microscopic coordination probed via photoluminescence. *J. Mater. Chem. C* **2015**, *3*, 3428–3437.
- (56) Geng, F. X.; Matsushita, Y.; Ma, R. Z.; Xin, H.; Tanaka, M.; Izumi, F.; Iyi, N.; Sasaki, T. General Synthesis and Structural Evolution of a Layered Family of Ln₈(OH)₂₀Cl₄·nH₂O (Ln = Nd, Sm, Eu, Gd, Tb, Dy, Ho, Er, Tm, and Y). *J. Am. Chem. Soc.* **2008**, *130*, 16344–16350.
- (57) Geng, F. X.; Matsushita, Y.; Ma, R. Z.; Xin, H.; Tanaka, M.; Iyi, N.; Sasaki, T. Synthesis and Properties of Well-Crystallized Layered Rare-Earth Hydroxide Nitrates from Homogeneous Precipitation. *Inorg. Chem.* **2009**, *48*, 6724–6730.
- (58) Mikhailik, V. B.; Kraus, H.; Miller, G.; Mykhaylyk, M. S.; Wahl, D. Luminescence of CaWO₄, CaMoO₄, and ZnWO₄ scintillating crystals under different excitations. *J. Appl. Phys.* **2005**, *97*, 083523.
- (59) Shi, X. F.; Li, J.-G.; Zhu, Q.; Li, X. D.; Sun, X. D. Hydrothermal assisted synthesis and photoluminescence of (Y_{1-x}Eu_x)₂WO₆ red phosphors. *J. Alloys Compd.* **2017**, *695*, 1984–1992.
- (60) Wang, X. J.; Li, J.-G.; Zhu, Q.; Li, X. D.; Sun, X. D.; Sakka, Y. Facile and green synthesis of (La_{0.95}Eu_{0.05})₂O₂S red phosphors with sulfate-ion pillared layered hydroxides as a new type of precursor: controlled hydrothermal processing, phase evolution and photoluminescence. *Sci. Technol. Adv. Mater.* **2014**, *15*, 014204.
- (61) Liu, Y.; Liu, G. X.; Wang, J. X.; Dong, X. T.; Yu, W. S.; Wang, T. T. Hydrothermal synthesis, multicolor tunable luminescence and energy transfer of Eu³⁺ or/and Tb³⁺ activated NaY(WO₄)₂ nanophosphors. *J. Mater. Sci.: Mater. Electron.* **2016**, *27*, 10780–10790.
- (62) Liao, J. S.; Zhang, S. A.; You, H. Y.; Wen, H.-R.; Chen, J.-L.; You, W. X. Energy transfer and luminescence properties of Eu³⁺-doped NaTb(WO₄)₂ phosphor prepared by a facile hydrothermal method. *Opt. Mater.* **2011**, *33*, 953–957.
- (63) Tu, D. T.; Liu, Y. S.; Zhu, H. M.; Li, R. F.; Liu, L. Q.; Chen, X. Y. Breakdown of crystallographic site symmetry in lanthanide-doped NaYF₄ crystals. *Angew. Chem., Int. Ed.* **2013**, *52*, 1128–1133.
- (64) Atuchin, V. V.; Aleksandrovsky, A. S.; Chimitova, O. D.; Gavrilova, T. A.; Krylov, A. S.; Molokeev, M. S.; Oreshonkov, A. S.; Bazarov, B. G.; Bazarova, J. G. Synthesis and Spectroscopic Properties of Monoclinic α-Eu₂(MoO₄)₃. *J. Phys. Chem. C* **2014**, *118*, 15404–15411.
- (65) Shi, P.; Xia, Z. G.; Molokeev, M. S.; Atuchin, V. V. Crystal chemistry and luminescence properties of red-emitting CsGd_{1-x}Eu_x(MoO₄)₂ solid-solution phosphors. *Dalton Trans* **2014**, *43*, 9669–9676.
- (66) Atuchin, V. V.; Subanakov, A. K.; Aleksandrovsky, A. S.; Bazarov, B. G.; Bazarova, J. G.; Gavrilova, T. A.; Krylov, A. S.; Molokeev, M. S.; Oreshonkov, A. S.; Stefanovich, S. Y. Structural and spectroscopic properties of new noncentrosymmetric self-activated borate Rb₃EuB₆O₁₂ with B₃O₁₀ units. *Mater. Des.* **2018**, *140*, 488–494.

(67) Atuchin, V. V.; Aleksandrovsky, A. S.; Chimitova, O. D.; Krylov, A. S.; Molokeyev, M. S.; Bazarov, B. G.; Bazarova, J. G.; Xia, Z. G. Synthesis and spectroscopic properties of multiferroic β - $\text{Tb}_2(\text{MoO}_4)_3$. *Opt. Mater.* **2014**, *36*, 1631–1635.

(68) Wang, X. J.; Li, J.-G.; Zhu, Q.; Sun, X. D. Direct Crystallization of Sulfate-Type Layered Hydroxide, Derivation of $(\text{Gd,Tb})_2\text{O}_3$ Green Phosphor, and Photoluminescence. *J. Am. Ceram. Soc.* **2015**, *98*, 3236–3242.

(69) Li, H.; Hong, G.; Yue, S. Investigation of $\text{NaLn}(\text{WO}_4)_2$ crystal ($\text{Ln} = \text{La, Pr, Nd}$). *Zhongguo Xitu Xuebao* **1990**, *8*, 37–41.

(70) Wang, H.; Li, Y. M.; Ning, Z. L.; Huang, L.; Zhong, C.; Wang, C.; Liu, M. J.; Lai, X.; Gao, D. J.; Bi, J. A novel red phosphor $\text{Li}_x\text{Na}_{1-x}\text{Eu}(\text{WO}_4)_2$ solid solution: Influences of Li/Na ratio on the microstructures and luminescence properties. *J. Lumin.* **2018**, *201*, 364–371.

(71) Wang, F.; Fan, X. P.; Pi, D. B.; Wang, Z. Y.; Wang, M. Q. Hydrothermal synthesis and luminescence behavior of rare-earth-doped $\text{NaLa}(\text{WO}_4)_2$ powders. *J. Solid State Chem.* **2005**, *178*, 825–830.